AGU PUBLICATIONS

JGR

Journal of Geophysical Research: Atmospheres

RESEARCH ARTICLE

10.1002/2017JD027589

Regional Responses to Black Carbon Aerosols: The Importance of Air-Sea Interaction

A. Gnanadesikan[1], A. A. Scott[1], M.-A. Pradal[1], W. J. M. Seviour[1], and D. W. Waugh[1]

[1] Department of Earth and Planetary Sciences, The Johns Hopkins University, Baltimore, MD, USA

Key Points:
- Anthropogenic carbon in a coupled climate model produces warming over land but cooling over the North Pacific
- Changes in atmospheric stabilization help drive temperature changes over land and ocean
- An associated slowdown in ocean circulation doubles the cooling impact of clouds over the North Pacific

Supporting Information:
- Supporting Information S1

Correspondence to:
A. Gnanadesikan,
gnanades@jhu.edu

Citation:
Gnanadesikan, A., Scott, A. A., Pradal, M.-A., Seviour, W. J. M., & Waugh, D. W. (2017). Regional responses to black carbon aerosols: The importance of air-sea interaction. *Journal of Geophysical Research: Atmospheres*, *122*. https://doi.org/10.1002/2017JD027589

Received 22 AUG 2017
Accepted 12 NOV 2017
Accepted article online 17 NOV 2017

Abstract The impact of modern black carbon aerosols on climate via their changes in radiative balance is studied using a coupled model where sea surface temperatures (SSTs) are allowed to vary and an atmosphere-only version of the same model where SSTs are held fixed. Allowing the ocean to respond is shown to have a profound impact on the pattern of temperature change. Particularly, large impacts are found in the North Pacific (which cools by up to 1 K in the coupled model) and in north central Asia (which warms in the coupled simulation and cools in the fixed SST simulation). Neither set of experiments shows large changes in surface temperatures in the Southeast Asian region where the atmospheric burden of black carbon is highest. These results are related to the stabilization of the atmosphere and changes in oceanic heat transport. Over the North Pacific, atmospheric stabilization results in an increase in stratiform clouds. The resulting shading reduces evaporation, freshening the surface layer of the ocean and reducing the inflow of warm subtropical waters. Over the land, a delicate balance between greater atmospheric absorption, shading of the surface and changes in latent cooling of the surface helps to determine whether warming or cooling is seen. Our results emphasize the importance of coupling in determining the response of the climate system to black carbon and suggest that black carbon may play an important role in modulating climate change over the North Pacific.

Plain Language Summary Particles of soot produced by combustion have greatly increased around the world over the last century and a half. As these particles absorb sunlight that might otherwise have been reflected back to space, they are believed to warm the planet as a whole. We tried to isolate the fingerprint of temperature change associated with soot (also known as black carbon) by taking a climate model and instantaneously increasing atmospheric concentrations from their 1860 values to modern values. The resulting pattern of temperature change looks very different than the pattern of atmospheric heating, with the largest warming found away from the most polluted regions and a region of cooling over the North Pacific. Changes in clouds, mixing, and ocean circulation all play a role in explaining these changes. In different regions these three processes have differing responses to the stabilization of the atmosphere produced by the additional heating at high altitudes. Over the North Pacific, the additional heating aloft reduces mixing of dry air into the near-surface boundary layer and shades the surface, increasing relative humidity and allowing for more stratus clouds. Reduced evaporation causes the surface waters to freshen, slowing the overturning circulation that supplies warm water to this region.

1. Introduction

Black carbon aerosols impact climate through a number of radiative, dynamical, and chemical processes. Produced by biomass burning and fossil fuel combustion, their presence in the atmosphere redistributes radiation through direct warming — by increasing shortwave absorption aloft — and cooling, as dimming reduces the amount of shortwave radiation reaching the surface (Bond et al., 2013). The net effect is to warm the planet, an effect which is more pronounced in the Northern Hemisphere than in the Southern Hemisphere (Bond et al., 2013). Indirect effects, such as microphysical changes in cloud nucleation or changes in cloud reflectivity (Twomey effect), and semidirect effects, referring to changes in cloud coverage forced by black carbon redistributing atmospheric heating (Non-Twomey-Albrecht Indirect Forcing or NTAIF), are other ways for black carbon to affect global climate. However, the extent to which these effects significantly modulate the impact of increased absorption on global mean temperature remains unclear (Bond et al., 2013).

Regional impacts are of particular interest because potential cooling effects can overwhelm warming effects on a local scale. In turn such local effects can have outsized influence on phenomena like monsoons or sea ice cycles. Many regional studies focus on South Asia precisely because its black carbon emissions are the highest in the world, finding that black carbon aerosols have a significant impact on the Indian summer monsoon (Meehl et al., 2008; Ramanathan et al., 2005; Wang et al., 2009). However, the effects of black carbon need not be localized to the region of emissions; indeed, inhomogeneous radiative forcing is known to have an influence on temperature thousands of kilometers away (Shindell et al., 2010), and black carbon can travel long distances once it reaches the upper troposphere.

Relatively few studies isolate the impact of black carbon in coupled ocean-atmosphere climate models, with many numerical studies using either a model with fixed sea surface temperature (SST) or a slab ocean model (Allen & Sherwood, 2010; Koch et al., 2011; Ramanathan et al., 2005; Roeckner et al., 2006). Of these, the last two are regional studies: Ramanathan et al. (2005) focus on India; Roeckner et al. (2006) look at the effects of redistributing aerosols from higher to lower latitudes. Fixing SST prevents the ocean from adjusting to the changes in regional climate and neglects feedbacks between ocean heat transport, SSTs, and the hydrological cycle, while slab ocean models neglect the effect of changes in ocean heat transport and mixed layer depth. A coupled ocean model is also critical to capture the effect of ocean circulation on radiative cloud feedbacks, particularly for low clouds (Trossman et al., 2016; Winton, 2003). Ocko et al. (2012, 2014) used historical simulations of the GFDL CM2.1 coupled climate model to compare and contrast the impacts of black carbon, sulfate, and organic carbon aerosols. While these simulations likely capture the impacts of aerosols in low latitudes, they may not do so in high latitudes where decadal variability can produce large-amplitude temperature anomalies that cannot be easily be distinguished from secular change with single, relatively short, historical simulations. Additionally, they do not specifically isolate the impact of coupling.

Tropospheric stabilization is an example of a localized effect which responds to ocean feedbacks and can be studied in models (e.g., Allen & Sherwood, 2010; Randles et al., 2013; Roeckner et al., 2006). As black carbon aloft absorbs solar radiation and warms the atmosphere, it creates an inversion layer and can alter cloud activity, particularly over convective regimes and marine areas. This is seen in observational studies that look at biomass burning events (Brioude et al., 2009; Keil & Haywood, 2003), although numerical studies show that the sign of the effect on cloudiness is unclear (Bond et al., 2013).

One numerical study (Persad et al., 2011) showed that the response to a spatially uniform black carbon layer differs according to the convective regime. Over convective regions they showed that the black carbon layer reduces the convective available potential energy, thus causing a reduction in convective mass flux. Over subsidence regions they found that the black carbon heating dries and lowers the boundary layer, reducing cloudiness above the boundary layer and increasing cloudiness within the boundary layer.

This paper presents the results of a sensitivity experiment in which black carbon aerosol levels are abruptly changed from preindustrial to modern levels, allowing for the resulting changes to be clearly distinguished from interannual variability. The change is made in both a fully coupled climate model and an atmosphere-only version of the same model with fixed SSTs, allowing us to diagnose the importance of oceanic feedbacks in determining the response. The equilibrium change is then studied, focusing in particular on the impact of semidirect forcing. We examine the changes in heating and cooling rates in different regions, highlighting important differences between land and ocean away from regions with large emissions. In keeping with previous work, we find that large black carbon aerosol concentrations in southeastern Asia cause heating across Eurasia and the Americas. However, several regional cold signals are detected, the most significant and novel of these occurring in the North Pacific, where as compared to preindustrial black carbon levels, SSTs cool by about 0.5 K and surface air temperatures cool by about 0.3 K. This previously unreported temperature response suggests a possible fingerprint for the impact of black carbon aerosols on climate.

2. Experimental Design

This experiment uses the Geophysical Fluid Dynamics Laboratory (GFDL) Earth System Model 2Mc (Galbraith et al., 2011) abbreviated as ESM2Mc. ESM2Mc is a coupled climate model with a fully interactive ocean and biogeochemistry module. The model is a low resolution (the atmospheric grid is 3.875° by 3°) version of GFDL Coupled Model 2 (CM2M) as described in Dunne et al. (2012) and is run with a diurnal radiation cycle. The atmospheric physics used in this model is described in Anderson et al. (2004), and the ocean physics is described in Griffies et al. (2005) and Gnanadesikan et al. (2006). A 2,500 year run is made with aerosols,

greenhouse gasses, and solar radiation fixed at year 1860 levels. Aerosols are prescribed from the off-line MOZART aerosol model (described in Horowitz et al., 2003) using aerosol emission and precursor estimates as described in Cooke et al. (1999) to produce a monthly climatology of aerosol concentration at all atmospheric levels. In addition to black carbon, the model includes sulfate (largely produced by ocean emissions), sea salt, and eight size classes of dust. Both the concentrations and resulting forcings produced from MOZART are more thoroughly evaluated in Ginoux et al. (2006). These aerosol concentrations are set to a climatological annual cycle in the models so that the model circulation does not affect the aerosol distribution. At 1800 years into the spin-up, we branch off an additional experiment with black carbon aerosols set to modern (calendar year 2000) levels. This experiment is run for an additional 300 years.

These relatively long simulations allow us to distinguish forced changes from long-period variability. Climatologies were computed from monthly means of the simulations (500 years for the control or preindustrial run, and 300 years for the experiment or black carbon run); changing the period of the climatology did not significantly affect results. We present differences between the two annual mean climatologies (black carbon minus control). Evaluation of whether differences with the control are significant is done by comparing with interannual variability at each grid point (computed from the 500 year control run) using a Student's t test corrected for autocorrelation at 95% confidence level. The model used here is a lower resolution version of that used in Ocko et al. (2012, 2014) but our use of a step function perturbation with long integrations gives us more confidence that we can distinguish small changes in high latitudes from interdecadal variability.

As sea surface temperature and cloudiness are not fixed, the model captures the semidirect or NTAIF forcing as well as dynamic feedbacks on clouds and ice due to temperature changes. However, aerosol indirect effects—for example, cloud nucleation and changes in cloud albedo—are not included. Moreover, clouds cannot change the aerosol distribution. The semidirect effect is thus isolated from other indirect effects in our experiment.

Changing black carbon aerosols produces both primary impacts on the local radiative balance and secondary impacts via changes in sea surface temperatures. To distinguish these two types of impact, we conducted a similar atmosphere-only experiment with fixed SSTs. A control simulation was made using annually repeating monthly climatological SSTs from the 1,860 coupled control simulation with preindustrial greenhouse gasses and aerosols. A parallel simulation was made where black carbon aerosols were set to modern (calendar year 2000) levels and integrated for 100 years. Comparing the fixed SST experiment with the fully coupled experiment is used to help isolate responses resulting from coupled air-sea interactions and to quantify the size of oceanic feedbacks that may either amplify or damp uncoupled changes.

Heating and cooling rate anomalies were calculated from the annual means of the climatology, following Persad et al. (2011). A particular focus of this paper is the effect of these anomalies on atmospheric stability. We note that a process that results in a uniform temperature increase at all pressure levels will actually increase stability because the potential temperature $\theta = T(p/p_0)^{-R/c_p}$ will increase more at low pressures than at high pressures. An increase in θ aloft relative to the surface thus signifies that air at the surface will need more energy to penetrate to the upper level. However, in monsoonal regions in particular decreases in the surface energy associated with cooling may be more than compensated by increases in latent heat energy associated with a greater inflow of moist air. For this reason we also look at vertical gradients in the moist potential temperature $\theta_m = \theta + L * q/c_p$ where L is the latent heat of vaporization, q is the specific humidity, and c_p is the specific heat at constant pressure. An increase in the difference in moist potential temperature between the surface and upper atmosphere means that the atmosphere has become more stable to penetrative convection.

The processes that can alter the atmospheric potential temperature profile include shortwave heating $\frac{\partial \theta}{\partial t}_{\text{sw}}$, longwave cooling $\frac{\partial \theta}{\partial t}_{\text{lw}}$, and vertical diffusion and turbulence $\frac{\partial \theta}{\partial t}_{\text{vdiff}}$, which when negative can be interpreted as diffusive cooling. Latent heat release from cloud formation is divided between that due to cumulus clouds generated by penetrative convection $\frac{\partial \theta}{\partial t}_{\text{cv}}$ and that due to stratiform or large-scale cloud formation $\frac{\partial \theta}{\partial t}_{\text{ls}}$. Cumulus convection (parameterized by the Relaxed Arakawa Schubert scheme, Moorthi & Suarez, 1992) transports parcels between grid boxes, whereas stratiform convection (Jakob & Klein, 2000; Moorthi & Suarez, 1992; Rotstayn, 1997; Rotstayn et al., 2000) forms or removes clouds within a large fraction of a grid box when moisture exceeds a certain threshold. On centennial time scales, the heat fluxes associated with temperature

trends are vanishingly small, so that any residual must be balanced by advection. We therefore compute the dynamical advection of sensible heat $\frac{\partial \theta}{\partial t}_A$,

$$\frac{\partial \theta}{\partial t}_A = -\left(\frac{\partial \theta}{\partial t}_{sw} + \frac{\partial \theta}{\partial t}_{lw} + \frac{\partial \theta}{\partial t}_{vdiff} + \frac{\partial \theta}{\partial t}_{cv} + \frac{\partial \theta}{\partial t}_{ls}\right) \quad (1)$$

as representing the heating or cooling from an air mass entering or leaving a region. Our approach differs from Persad et al. (2011) in that they looked at local heating terms $\partial T/\partial t$ while we focus on $\partial \theta/\partial t = \partial T/\partial t(p/p_0)^{-R/c_p}$.

3. Results

We divide the results from our simulations into four parts. Before considering the impacts of black carbon, we first consider how the control simulates the hydrography of the North Pacific in section 3.1. The realism of the oceanic simulation of this region has not been evaluated in previous work describing results from ESM2Mc. In section 3.2 we then consider the large-scale patterns of changes in temperatures and circulation induced by adding black carbon to both coupled and fixed SST models and highlight three regions with very different responses than we might naively expect. Section 3.3 examines term balances to identify what processes heat and cool each region. Finally, section 3.4 considers the role of air-sea coupling in amplifying cooling in the North Pacific.

3.1. Evaluation of the Control Model in the North Pacific

The observed zonally averaged temperature in the North Pacific for the decade of 1965–1974 (Locarnini et al., 2013, Figure 1a) shows a thin layer of warmer water extending into the subpolar gyre from the subtropics, with interior waters between 2 and 4°C. With the caveat that the control model represents preindustrial conditions, it nonetheless reproduces this broad-scale pattern relatively faithfully (Figure 1b), although the warm subtropical water penetrates further into the subpolar gyre in the observations. Cross sections of temperature in the middle of the subpolar gyre at 55°N (Figures 1c and 1d) show the penetration of warmer waters in the eastern gyre with colder waters in the west. While there are differences in detail, the picture is qualitatively reasonable. Observed salinity (Figure 1e) shows a relatively strong halocline in the North Pacific, with relatively fresh and cold waters (potentially indicative of intermediate water formation) penetrating to depths of about 600 m. Modeled salinity (Figure 1f) shows a weaker halocline, with somewhat deeper penetration of the fresh signal than in the observations.

The meridional overturning circulation associated with this hydrography is shown in Figure 2a (positive contours denote clockwise circulation, negative counterclockwise circulation). The boundary between the subtropical and subpolar gyres (defined as the line of zero wind stress curl) lies at about 43°N in the model. There is a northward net flow of more than 6 Sverdrup (Sv) across this latitude between depths of 100 and 400 m. About half of this flow is returned in the surface layer, while the remainder is returned at depth as North Pacific Intermediate Water. The estimated deep overturning here is somewhat smaller than the 5 Sv estimated in Talley (1999). A cross section of the flow at the nearest grid point to the north (Figure 2b) shows that the northward flow is associated with a warm jet at about 140°W, with the return at depth occurring in much colder water at the western boundary. Because some of the southward flow occurs at the same depth as the northward flow, it will not be captured by the overturning stream function. The total advective heat flux across this section (carried by both the horizontal and vertical circulations) is around 0.25 PW.

3.2. Impacts of Black Carbon Aerosol: Large-Scale Patterns

We now turn to the response within the models to a step change in black carbon aerosol. Figure 3a shows the annual average column-integrated distribution of black carbon (year 2000 levels from Ginoux et al., 2006) in mg m^{-2}. Black carbon concentrations are larger in the Northern Hemisphere than in the Southern Hemisphere. Over "southeastern Asia" (here we mean the nonpolitical region that is south and east of central Asia) the concentrations exceed the global mean by approximately 1 order of magnitude, reflecting modern day heterogeneous emissions patterns. This region includes much of the most populated area of China. The emissions data set used in the MOZART model results in an overestimate of black carbon in polluted areas with respect to remote observations and in situ measurements (Ginoux et al., 2006). In the North Pacific region, the resulting local concentrations fall within the range of black carbon concentrations from AeroCom II models but are on the larger end and also exceed recent aircraft observations (Samset et al., 2014). However, given the large uncertainties in the observations and the fact that these black carbon concentrations have been used

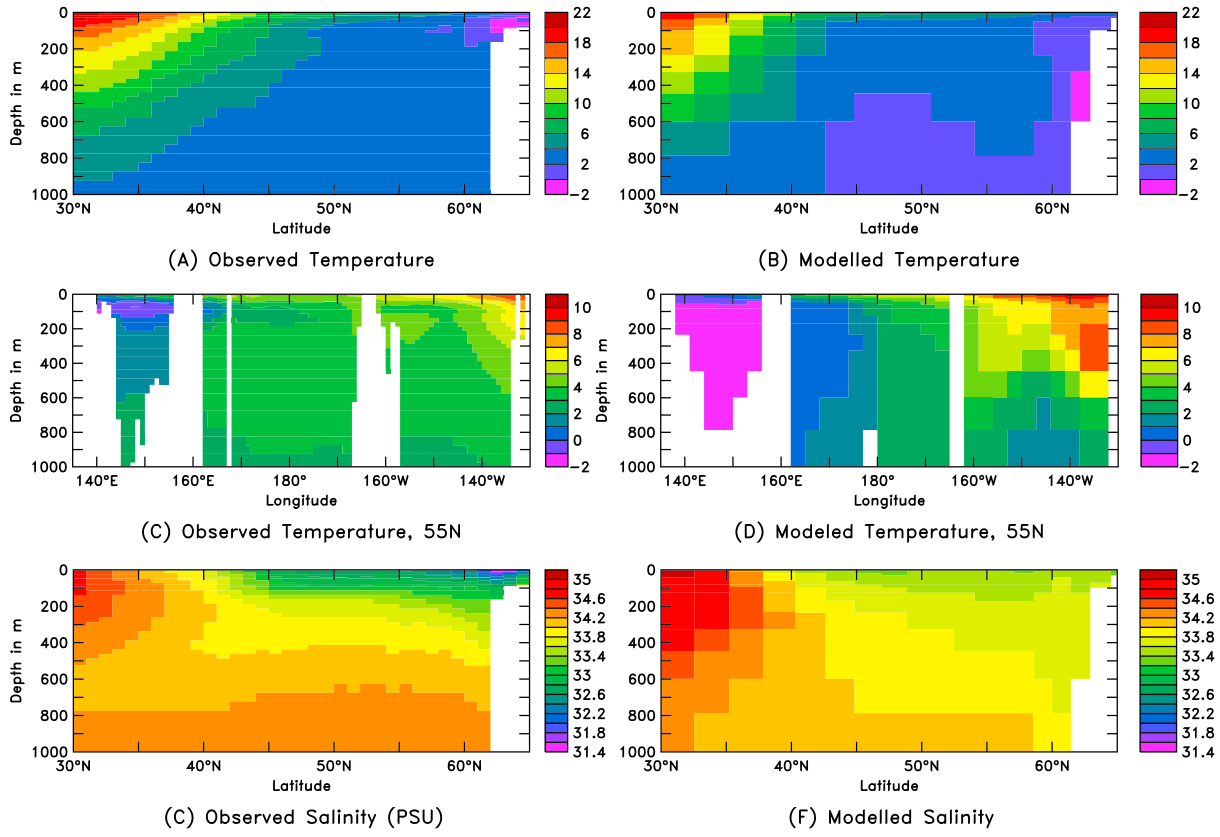

Figure 1. Hydrography of the North Pacific in climatology of the Control (preindustrial) model. (a) Observed zonally averaged temperatures for the decade of 1965–1974 from the World Ocean Atlas 2013 (Locarnini et al., 2013). (b) Modeled zonally averaged temperatures. (c) Observed temperature at 55°N. (d) Modeled temperature at 55°N. (e) Observed zonally averaged salinity for the decade of 1965–1974 (Zweng et al., 2013). (f) Modeled zonally averaged salinity.

to drive runs made as part of the Intergovernmental Panel on Climate Change Fifth Assessment Report, our sensitivity study is still relevant for understanding the impact of black carbon in model simulations.

We begin by examining results from the coupled simulations. The addition of black carbon increases the absorption of radiation by the atmosphere. The change in the net clear-sky shortwave (SW) atmospheric heating is shown in Figure 3b and has a global average of 2.4 W/m^2. Total sky changes are very similar to the clear-sky changes (with a correlation of 0.99 and RMS difference of 0.27 W/m^2). Although the pattern of atmospheric heating should also be changed by differences in water vapor, we note that atmospheric heating changes match the distribution of black carbon closely (correlation coefficient 0.99). The correlation with

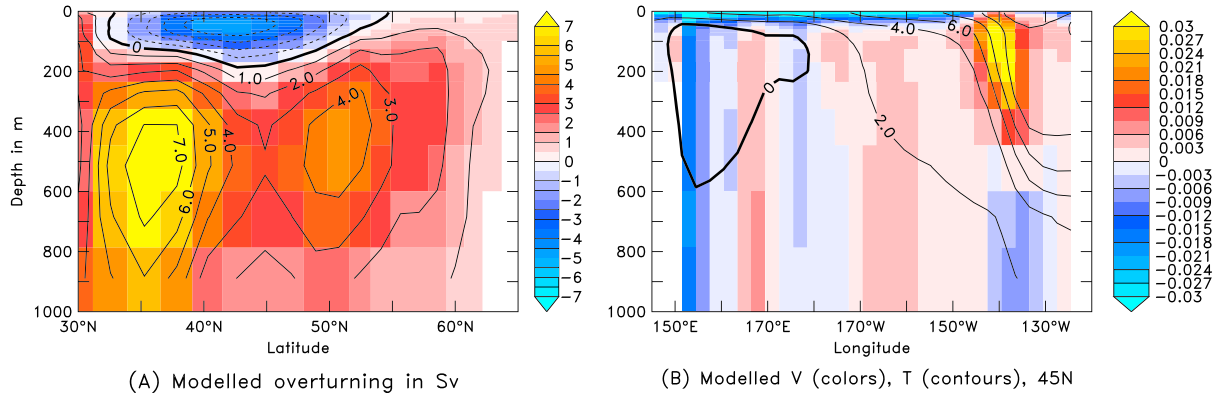

Figure 2. Modeled North Pacific flow in Control. (a) Overturning circulation in Sv (positive is clockwise), negative is counterclockwise). (b) Cross section of north-south velocity in m/s (colors) and temperature (contours) at 45°N, close to the southern boundary of the subpolar gyre.

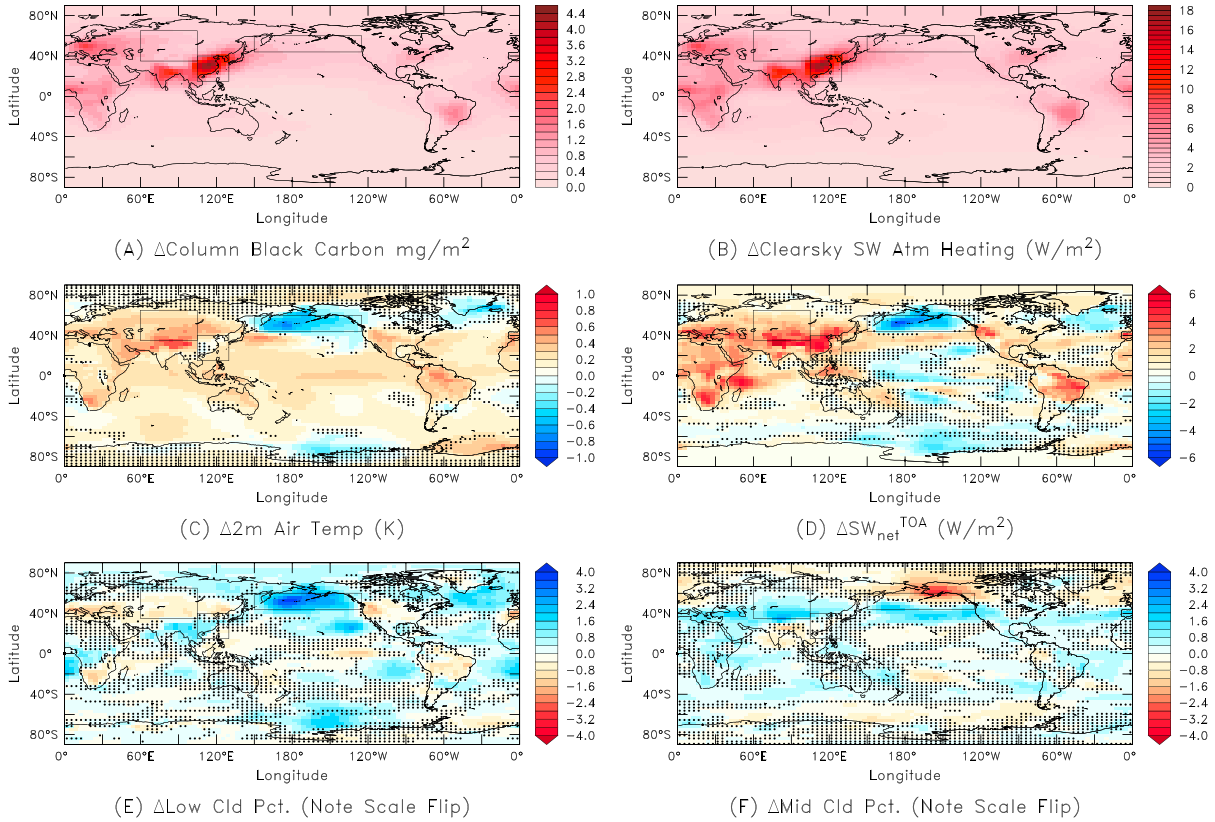

Figure 3. (a) Black carbon concentration (column integrated and time averaged), (b) resulting change in net clear-sky shortwave atmospheric heating, (c) 2 m air temperature changes, (d) net incoming SW radiation at the top of the atmosphere (positive values indicate warming), (e) low-level and (f) midlevel cloudiness. Dots indicate areas where results fail to rise above the 95% statistical significance relative to unforced variability. The three boxes define areas to be analyzed in Figures 6–11.

changes in water vapor pathway is only 0.27, suggesting that water vapor feedbacks play a secondary role. Black carbon concentrations are greatest in India and southeastern Asia, so accordingly, both clear-sky and total sky SW heating are greatest in this same region.

As some of the additional radiation heating the atmosphere would have been absorbed at the ground, the net incoming radiation is less strongly impacted than the atmospheric heating by itself. The change in clear-sky top of the atmosphere (TOA) net incoming SW radiation is +0.64 W/m^2, while the total sky change is +0.89 W/m^2. Bond et al. (2013) find an instantaneous clear-sky forcing of +0.7 W m^{-2}. As this is calculated by computing the change in radiative heating without allowing water vapor or surface albedos to change it is conceptually closest to our calculated clear-sky change. The good degree of agreement reassures us that the model is not applying completely unrealistic levels of forcing.

We might naively expect that increasing black carbon would be a good predictor of local surface warming. The equilibrium 2 m temperature change (Figure 3c) shows that this is not the case. Positive temperature anomalies, the expected result, are balanced by cooling signals in several marine regions. In the Northern Hemisphere, centers of positive surface air temperature anomaly are centered north of the Himalayas with a tongue extending over the Pacific, over Europe, and over the United States and Mexico. In the northern Pacific, a region of near-surface atmospheric cooling of about 0.5 K (reflecting up to 1.2 K changes in SST, as seen in Figure S1 in the supporting information) is seen that extends into North America and to a lesser extent Asia. A similar zone of anomalous cooling is present over the North Atlantic and Greenland with a magnitude of up to 0.5 K in SST and 0.3 K in surface air temperature. The correlation between the change in black carbon column burden and surface air temperature change is only 0.17.

The changes in the net incoming SW radiation at the top of the atmosphere (Figure 3d, representing the total energy absorbed by atmosphere, land, and ocean) match the surface air temperature changes much better

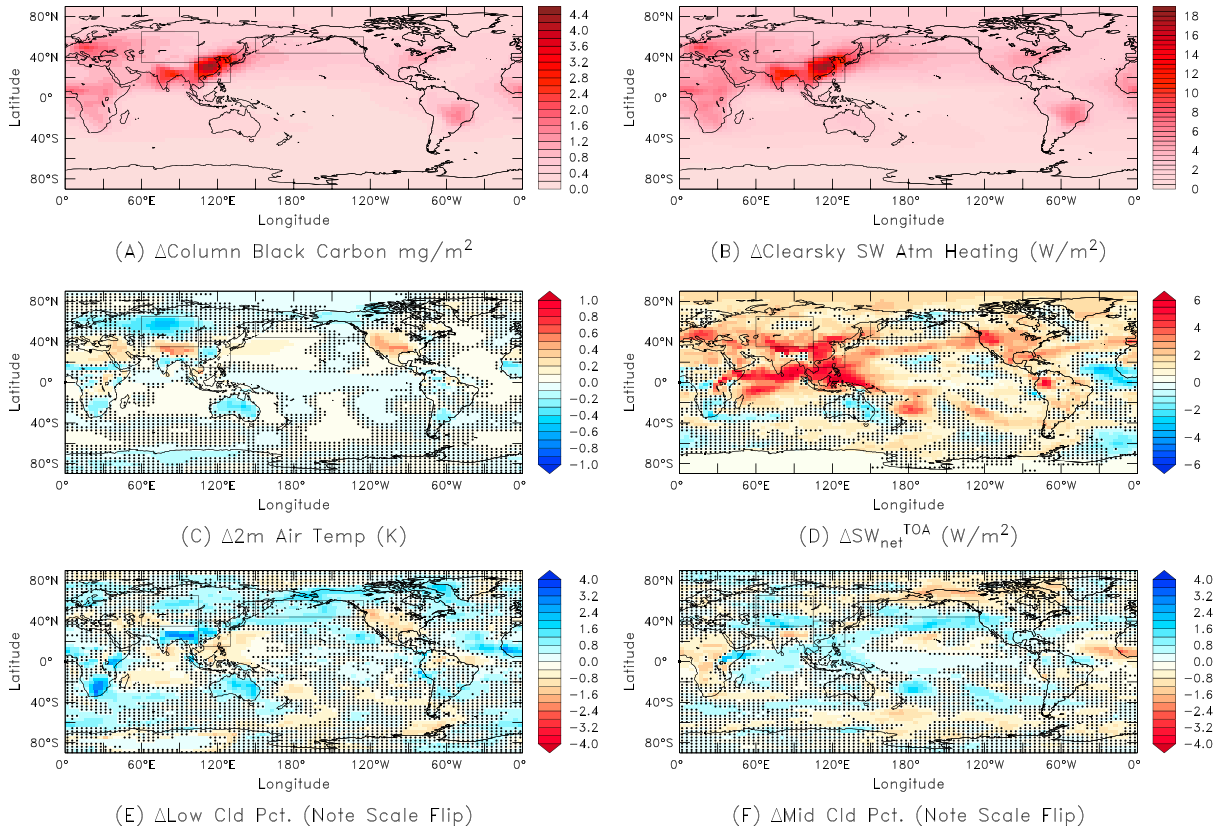

Figure 4. For fixed SST experiment: (a) column-integrated black carbon (time averaged) and (b) resulting change in net clear-sky shortwave atmospheric heating, (c) 2 m air temperature changes, (d) net incoming shortwave radiation at the top of the atmosphere (positive values indicate warming), (e) low-level and (f) midlevel cloudiness. Dots indicate areas where results fail to rise above 95% statistical significance relative to unforced variability. The three boxes define areas to be analyzed in Figures 6–11.

than the changes in atmospheric heating (Figure 3b). The TOA net incoming SW changes show a correlation of 0.57 with temperature change, while the atmospheric heating change is much more weakly correlated (0.13). This suggests that understanding the surface air temperature response requires understanding how the clouds change in response to heating, as previously found in fixed SST simulations by Randles et al. (2013). In the coupled simulations changes in low-level clouds are spatially anticorrelated (−0.68) with temperature changes, with increases over the North Pacific and over southeastern Asia, and decreases over central Asia. Midlevel clouds are more weakly anticorrelated (−0.30) with surface changes but may contribute to continental warming. High cloud changes show an insignificant correlation (0.09) with surface temperature changes and are not shown here. The fact that changes in low clouds appear to be key in explaining the temperature pattern further motivates our focus (developed further in section 3.3) on characterizing how the heating caused by black carbon changes the stability of the lower atmosphere.

The fixed SST simulations (Figure 4) show an identical picture for the changes in black carbon (as the same change is specified in both sets of simulations) and an essentially identical picture (correlation coefficient of 0.98) for the total atmospheric heating. The changes in surface air temperature, however, are very different, even when only areas over land are considered (correlation coefficient with the coupled model SAT changes is 0.21). The SAT changes have a linkage to TOA shortwave forcing (correlation coefficient of 0.52) when land areas alone are considered, similar to that seen for the coupled model. The linkages to low clouds are weaker than in the coupled case (correlation coefficient of −0.41 with land areas alone considered), as are those for midlevel clouds (−0.13 with land areas alone considered) . Relative to the coupled simulations both of these cloud fields exhibit different patterns of change in the fixed SST runs, particularly over the North Pacific.

It is informative to compare the dynamical response of the coupled and fixed SST simulations to adding black carbon. As shown in Figures 5a and 5b both sets of simulations show an increase of about 2 mbar in North Pacific surface pressures, with outward spiraling winds at a reference height of 2 m indicating a reduction of

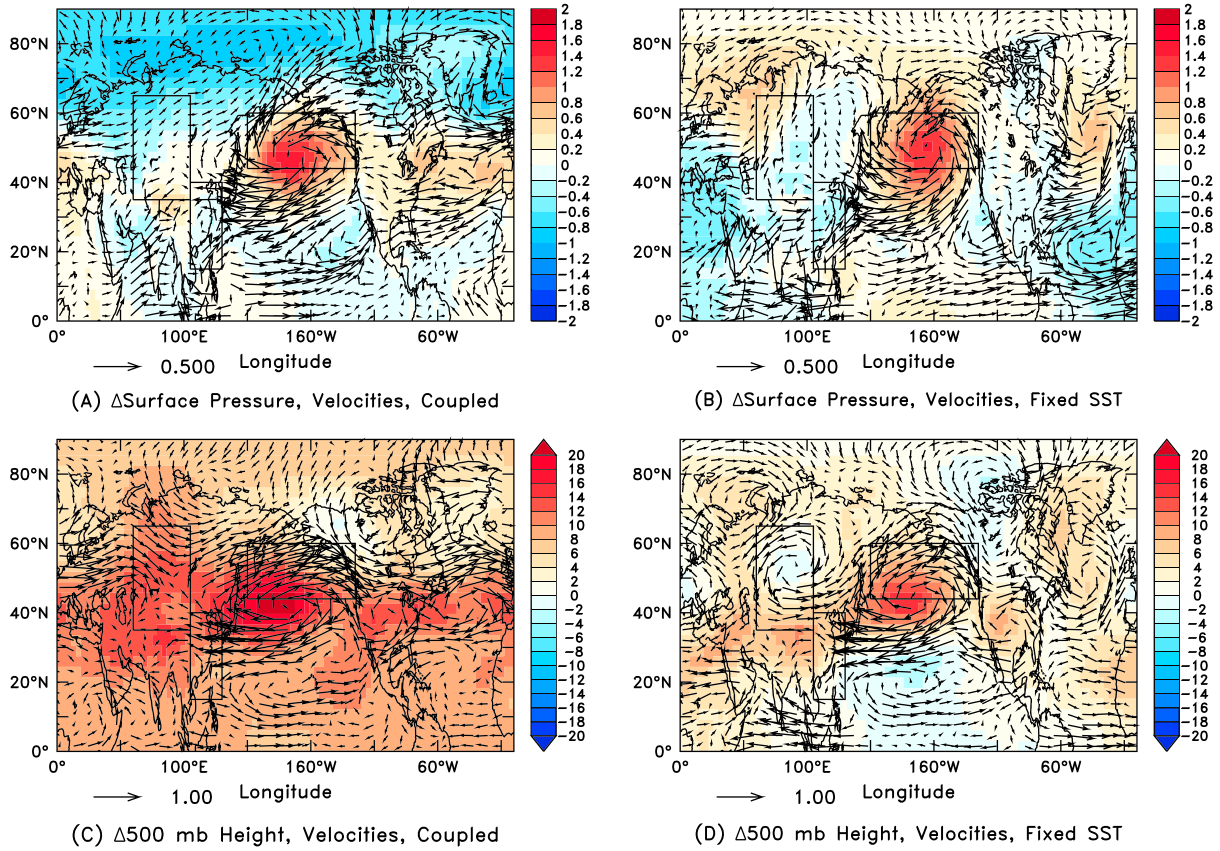

Figure 5. Dynamical changes at surface (top row) and 500 mbar (bottom row) due to adding black carbon in the coupled (left column) and fixed SST (right column) simulations. The three boxes define areas that are analyzed below. (a) Change in surface pressure in mbar (colors) and winds at 2 m (vectors), coupled models. (b) Change in surface pressure in mbar (colors) and winds at 2 m (vectors), fixed SST models. (c) Change in height of the 500 mbar surface (colors) and winds in m/s at 500 mbar (vectors), coupled models. (d) Change in surface pressure in mbar and winds in m/s at 500 mbar (vectors), fixed SST models.

convergence in the Aleutian low. The fact that this signal is found in the fixed SST simulations indicates that the coupled response is not simply due to a dynamical response to the relatively small changes in tropical temperature seen in Figure 3c. This is worth noting because relatively small changes in tropical temperatures and temperature gradients can have disproportionate impacts on extratropical circulations—see, for example, Seager et al. (2005). Away from the North Pacific the pattern of 2 m wind changes is quite different, particularly over north central Asia. In this region, the effect of adding black carbon in the coupled simulations is to produce stronger surface inflow in the northwest and stronger surface outflow at the north. However, in the fixed SST simulations, adding black carbon results in the opposite behavior. At 500 mbar (Figures 5c and 5d) the coupled model shows the impact of tropical warming raising the atmospheric temperatures below this level by about 0.3 K, raising the height of this level by around 6 m. The overall pattern of changes in 500 mbar height and velocities over the Pacific in particular is quite similar in both coupled and fixed SST simulations. Both pairs of simulations show an increase in 500 mbar height that is offset slightly to the south of the increased surface pressure. The circulation about this anomalous high has a similar magnitude (peak wind changes around 1 m s^{-1}) in both sets of simulations.

3.3. Regional Responses and Heating Rate Balances

In order to develop a better process-based understanding of the regional response we first choose regions with different behavior and examine budgets within each region. We note at the outset that attributing causality to term balances is not straightforward, as the largest warming process at some point may not be fully resolved by the diagnostics (i.e., additional longwave absorption and reradiation at a model grid point could give a warming with little net heating). Additionally, as we will see, the process with the largest impact on a given point may be a response to other changes in heating. However, we note that changes in the concentration of absorbers can be expected to affect radiative heating and that it makes little sense to attribute

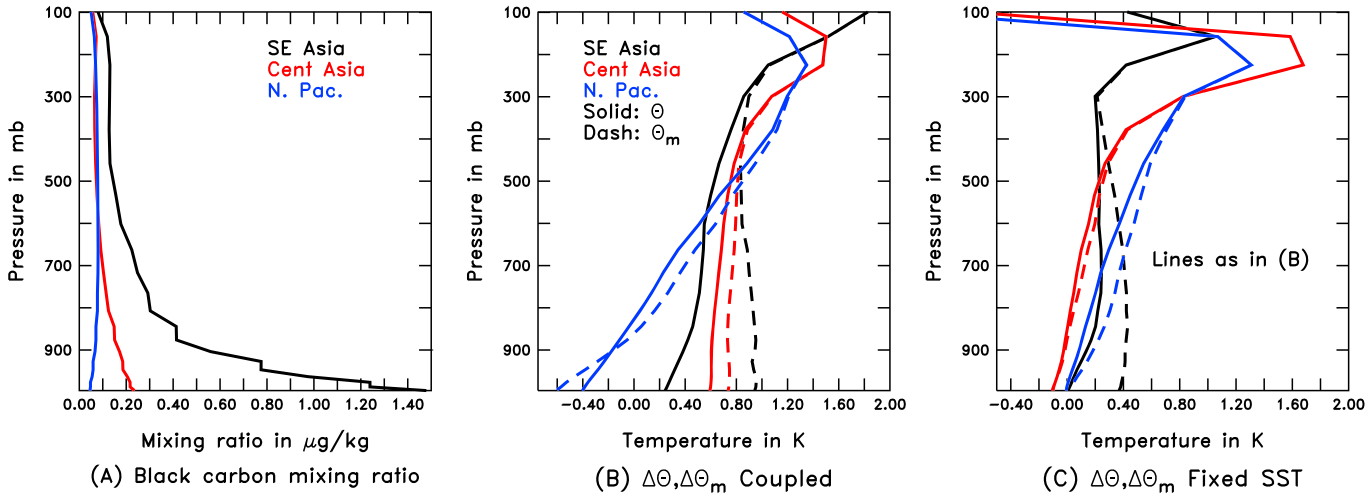

Figure 6. Regional changes. Black lines show Southeast Asian region where peak column-integrated black carbon concentrations are found (105–130°E, 15–40°N). Red lines show central Asian region which shows surface warming in the coupled simulation (60–105°E,35–65°N). Blue lines show North Pacific region where there is a cooling in the coupled simulation (150°E–125°W, 44–60°N). (a) Black carbon. (b) Potential temperature (solid) and moist potential temperatures (dashed) in coupled simulations. (c) Potential temperature (solid) and moist potential temperature (dashed) in fixed SST simulations.

a warming in some region (shown in Figures 6b and 6c) to a process which is cooling that region (shown below in Figure 7). Three regions (delimited by the black boxes in Figure 3) are isolated for further analysis: the region in southeastern Asia from whence the majority of the forcing originates, between 15°N–40°N and 105°E–130°E, the warming region over land in central Asia, between 35°N–65°N and 60°E–105°E, and the cooling region over the North Pacific, between 44°N–60°N and 150°E–125°W.

We begin by examining profiles of black carbon aerosol mixing ratio, potential temperature θ, and moist potential temperature $\theta_M = \theta + L * q/c_p$. Vertical profiles averaged over each region show that the surface black carbon concentration (Figure 6a) changes by the most in the SE Asia region (as would be expected given the level of industrial activity there) and by the least in the North Pacific region. Above about 400 mbar, the mixing ratio changes in different regions are much more similar. At 379 mbar the mixing ratios in SE Asia, north central Asia, and the North Pacific are 0.127, 0.066, and 0.076 μg kg^{-1}, respectively, while near-surface mixing ratios vary by more than a factor of 30. Looking at the changes in potential temperature in the coupled model (solid lines, Figure 6b) we see that there are somewhat similar changes across regions in the upper atmosphere, which warms by more than 1 K in all three regions. However, the lower atmosphere changes do not reflect the differences in black carbon between the regions. The Southeast Asia region warms slightly, but the potential temperature change lies between central Asia and the North Pacific below 600 mbar. In general, the changes in potential temperature are consistent with an increase in atmospheric stability.

The changes in θ_m (dashed lines, Figure 6b) show some interesting differences from the changes in θ. First, they show a larger increase over Southeast Asia, a smaller increase over central Asia, and a cooling over the North Pacific, consistent with ordering of the differences in shortwave forcing. The moist potential temperature also shows a stabilization of the atmospheric column over the North Pacific as the difference between 400 mbar and the surface is larger by about 1.2 K. Over Southeast Asia, the difference between the surface and 400 mbar decreases by about 0.2 K, implying weak destabilization. The fixed SST simulations (Figure 6c) show qualitatively similar changes in atmospheric stability in the North Pacific and Southeast Asia. Over central Asia (red lines), the fixed SST simulations show a decrease in temperature, no change in specific humidity and thus an increase in atmospheric stability. By contrast, the coupled simulations show a warming but essentially no change in vertical gradient and thus in stability.

In order to understand why the differences in concentration do not map simply onto changes in temperature we now turn to the regional heating rate (Figure 7) and surface heat flux (Table 1) balances, starting with Southeast Asia. Below 850 mbar, the additional SW heating of the atmosphere (Figure 7a, dark blue curve) associated with greater aerosol concentrations is balanced by less heat diffusing upward from the ground (red curve). This suggests that instead of SW radiation being absorbed by the ground and the absorbed energy then getting mixed upward into the atmosphere, it is simply absorbed locally. The net change of net

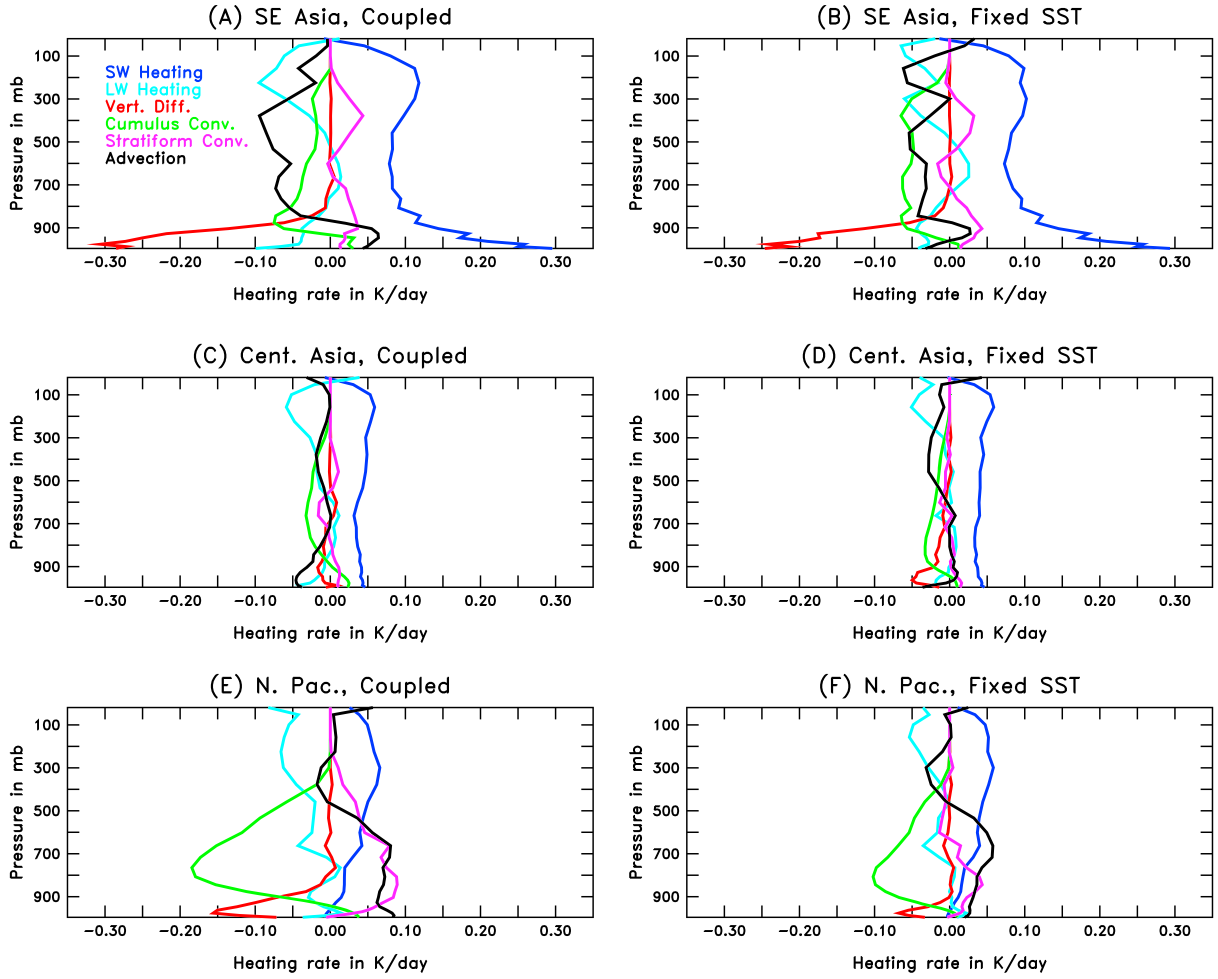

Figure 7. Change in column energy budget by region. (a, c, and e) Results for coupled simulations and (b, d, and f) results for fixed-SST simulations. SE Asia region with large black carbon column burden (Figures 7a and 7b). North central Asian region where there is warming in the coupled simulation (Figures 7c and 7d). North Pacific region with cooling in the coupled simulation (Figures 7e and 7f).

downward SW radiation at the surface in this region is −6.3 W m^{-2} (Table 1). This is more than sufficient to account for the −3.1 W m^{-2} drop in sensible heat flux and −2.8 W m^{-2} drop in the diffusive heating below 900 mbar. By contrast the additional absorption of shortwave radiation below 900 mbar is only 2.4 W m^{-2}. Near-surface temperatures only rise because changes in circulation (black curve) bring in warmer and moister air. The increase in moisture (shown by the increase in moist versus dry potential temperature in Figure 6b) causes the latent cooling of the surface to drop by 2.8 W m^{-2} and allows the surface to warm. The failure of the SE Asia region to show a large rise in temperatures is thus primarily due to shading from black carbon, ameliorated in part by changes in circulation.

The heating rate balances are very different as we move up in the atmosphere. The impacts of the circulation change are also seen in the free troposphere (between 250 and 800 mbar). In this region the concentration of black carbon falls away rapidly and the SW heating rate drops. The added heat is largely advected away (black curve, Figure 7a). The largest temperature changes are found above 300 mbar, where increased SW heating is balanced by increased LW cooling (light blue). There appears to be a switch from cumulus (green line) to stratiform convection (purple line) over two ranges of pressure, 300–500 mbar and 700–900 mbar. This switch is consistent with greater dry static stability suppressing penetrative convection- though it should be noted that the increase in moisture throughout the troposphere seen in Figure 6b would be expected to oppose such an effect.

We note that the shortwave heating in SE Asia (blue curve, Figure 7a) shows much less contrast between the surface and 200 mbar (with 200 mbar heating rates 26% of surface heating rate) than does the black carbon

Table 1
Changes Insurface Heat Fluxes in W m^{-2}, Black Carbon-Control for Three Regions

Flux/Exp	SE Asia coupled	SE Asia fixed-SST	NC Asia coupled	NC Asia fixed-SST	N Pac coupled	N Pac fixed-SST
Shortwave	−6.3	−5.7	−0.35	−1.2	−5.7	−3.0
Longwave	1.7	1.5	−0.66	−0.07	2.9	0.64
Sensible	3.1	2.5	0.31	0.46	1.7	0.06
Latent	2.8	3.0	0.61	0.74	4.0	0.94
Ocean heat transport	−1.3	0	0	0	−3.0	0.0

Note. Positive is out of atmosphere, into land or ocean.

mixing ratio (black curve, Figure 6a, with black carbon mixing ratios at 200 mbar 9% of surface values). This threefold difference in heating rate arises for two basic reasons. The first is that we are looking at changes in the rate of change of potential temperature which means changes in heating aloft are much more effective than at the surface. Weighting the heating rate by $(p/p_0)^{-R/c_p}$ accounts for a factor of 1.6 at 200 mbar and largely accounts for the increase in heating rates relative to 300 mbar. The second is that the net impact of clouds and aerosols is to increase the ambient radiation at 200 mbar as more radiation is reflected from below but to decrease it near the surface, so that the sum of upwelling and downwelling shortwave fluxes at 200 mbar is about twice that of those at the surface. Since black carbon heating depends on both the upwelling and downwelling fluxes, the changes in mixing ratio are twice as effective at producing heating at 200 mbar than they are at the surface.

In the region of warming in north central Asia, the simplest balance is again found at high altitude (above 200 mbar) where an increase in shortwave heating (Figure 7c, dark blue) is balanced by an increase in longwave cooling (light blue). At levels between 200 and 600 mbar, the excess SW heating is balanced by a combination of advective cooling (black), longwave cooling, and a decrease in condensational heating associated with cumulus convection (green). In the lower free troposphere (600–850 mbar), the increased shortwave heating is primarily balanced by the decrease in cumulus convection. Convection homogenizes energy in the atmosphere by moving surface air with greater moist static energy upward, so reducing cumulus convection cools at the altitudes where condensation occurs (here 600–850 mbar) and warms the boundary layer. Below 850 mbar, the increased heating from greater shortwave absorption and less cumulus convection is largely carried away by advection. Note that in this region the changes in stratiform heating are much smaller than the changes in heating from cumulus convection. As a result total cloud heating drops—as does low cloud amount (Figure 3e). This drop in low cloud amount compensates more than half of the −1.1 W m^{-2} drop in absorbed surface solar radiation under clear-sky conditions—the all-sky downward shortwave flux change is −0.35 W m^{-2}. In contrast to SE Asia, the increased atmospheric shortwave heating below 900 mbar—amounting to about 0.5 W m^{-2}—is not strongly offset by less vertical diffusive heating. Below 900 mbar the cooling from reduced upward diffusion of heat is only −0.11 W m^{-2}. Moreover, as in SE Asia an increase in moisture over this region (seen in the difference between the red lines in Figure 6b) results in less evaporation, heating the surface by 0.61 W m^{-2}. The net impact of the reduced evaporation, reduced cumulus convection, and increased near-surface shortwave heating is thus to warm the surface and boundary layer.

In the North Pacific, changes in cumulus convective heating become more important than changes in SW heating resulting from increasing aerosols. The changes in heating due to increased shortwave absorption are smaller than cooling processes over most of the lower troposphere; the net effect is to stabilize the atmosphere (as seen by the increase in potential and moist potential temperature gradients in Figure 6b). Thus, although the black carbon mixing ratio (Figure 6a, blue) is at a maximum around 700 mbar, there is a negative temperature response below 700 mbar. This response exceeds −0.3°C in the middle of the grid box closest to the surface. However, higher in the atmosphere, we see a warming of 1.2°C at 200 mbar. The response in θ_M shows that changes in moisture slightly amplify the resulting change in stability in the lower troposphere. Above 200 mbar, the heating balance (Figure 7e) is qualitatively similar to both of the other regions, with a smaller SW heating (blue) being balanced by LW cooling (light blue). Below this (400–900 mbar), the largest change is a drop in deep convective heating (green) that is not primarily balanced by a large increase

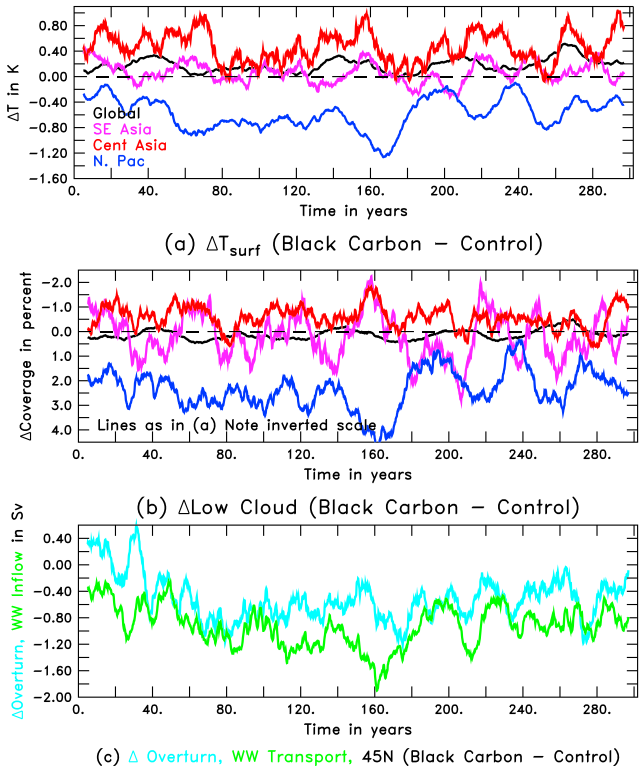

Figure 8. Time series of changes in various fields dein coupled simulation. (a) Temperature in different regions. (b) Low cloud cover in same set of regions (note inverted scale). (c) North Pacific overturning circulation (blue) and northward flow of water warmer than 6°C (green) at 45°N.

in shortwave heating. Instead, the reduction in deep convective heating is balanced by advection (black) and increased condensation associated with stratiform convection (purple). Note that the increase in stratiform convective heating is also associated with an increase in low cloud amount (Figure 3e). Below 500 mbar, advection acts to move warm air into the cooling region, mitigating the impact of the reduction in cumulus convection.

The increase in cloudiness reduces the amount of sunlight absorbed by the subpolar North Pacific Ocean (Table 1), reducing surface temperatures (Figure 3c). In the absence of clouds the downward shortwave radiation over this region drops by 2.3 W m^{-2}, whereas with clouds the drop is 5.7 W m^{-2}. This shows that when the boundary layer is stabilized in the presence of moisture, the result is to cool the surface and lower atmosphere rather than warm (consistent with Persad et al., 2011). Over the North Pacific between 20 and 65°N changes in low cloud are relatively well correlated (+0.65) with changes in the potential temperature difference between 700 and 1,000 mbar (a measure of the boundary layer dry stability). They are even better correlated (+0.73) with changes in the moist potential temperature difference between 700 and 1,000 mbar (a measure of the moist stability). By contrast, changes in the moisture convergence below 850 mbar are essentially uncorrelated with the change in cloudiness (+0.09). This suggests that it is the changes in stability rather than the changes in circulation that are primarily responsible for the changes in cloudiness. This result also holds for the fixed SST simulations.

In summary although all three regions see increased atmospheric heating from black carbon, the balances that result differ sharply between them. In SE Asia the increased shading produced by black carbon more than compensates the increased heating near the ground and changes in circulation must be invoked to bring in heat and balance net diabatic cooling. In north central Asia, the shading is much weaker and the increased heating of the atmosphere as well as circulation changes that moisten the atmosphere result in a warming. Over the North Pacific an increase in cloudiness associated with greater atmospheric stability produces a net cooling at the surface.

Comparing the regional heat balances in the coupled model with those in the fixed SST simulations (Figures 7b, 7d, and 7f) our first impression is that the patterns of change are quite similar. This is particularly true for the shortwave heating term. However, a number of differences are seen. The biggest of these is over the North Pacific Ocean, where the decline in cumulus convective heating and increase in stratiform convective heating is much larger in the coupled model. An additional surprising and very subtle difference is found over north central Asia. From the changes in circulation in Figures 5a and 5b, one might have expected that changes in advection were responsible for the near-surface cooling in the fixed SST case simulations. However, the advective heating (black line) in the fixed SST case is actually less negative than in the coupled case, suggesting that it is actually working to damp out the temperature anomaly. Instead, it is the vertical diffusive flux that is negative. The fixed SST simulation sees a −1.2 W m^{-2} drop in the surface shortwave absorption over north central Asia, more than 3 times as large as in the coupled simulation. As a result, a much greater fraction of the increased atmospheric SW heating below 900 mbar (+0.48 W m^{-2}) is compensated by less heat diffusing up from below (−0.33 W m^{-2}), making north central Asia in the fixed SST simulation look more like SE Asia in the coupled simulation.

One question given the size of the changes seen here is whether they might be explicable simply as a result of large-amplitude natural variability that has not been sufficiently averaged or be part of a transient adjustment. Figure 8a shows the time series of surface temperature globally (black) line, as well as in the three regions on which we have been focusing. While the basic patterns (net warming over the globe and central Asia, net cooling over the North Pacific, and small changes over Southeast Asia) are rapidly established, there is clear decadal variability in all signals. Variability in low clouds (shown with an inverted scale in Figure 8b) is strongly anticorrelated with the temperature differences both globally (−0.91) and regionally (−0.86 in SE Asia, −0.53

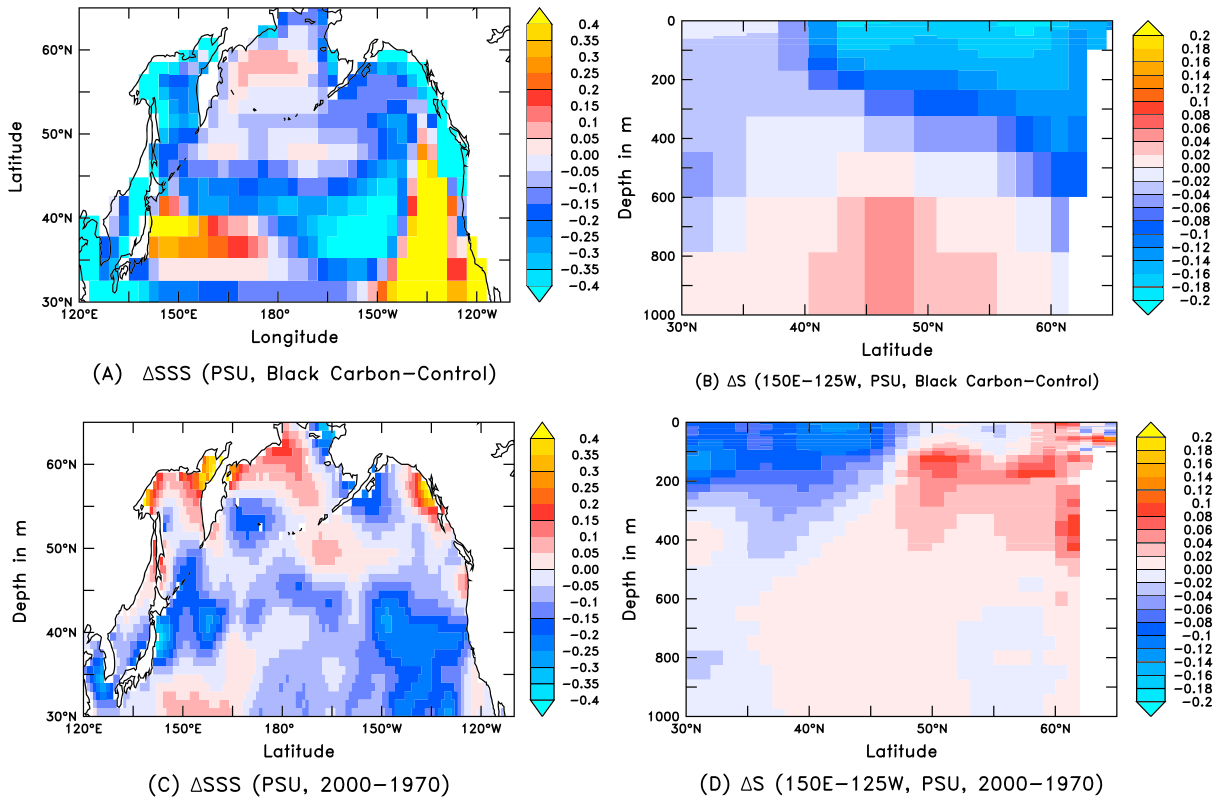

Figure 9. North Pacific salinity changes. (a) Simulated change in sea surface salinity from coupled simulation. (b) Zonally averaged change in salinity from coupled simulation. (c) Historical change in sea surface salinity from World Ocean Atlas 2013 (average from 1995 to 2004)−(average from 1964 to 1974). (d) Historical change in zonally averaged salinity from World Ocean Atlas 2013 (average from 1995 to 2004)−(average from 1964 to 1974).

in north central Asia, and −0.81 in the North Pacific). There is no sense from any of the curves of a long-term trend in clouds or SST, suggesting that the model achieves equilibrium relatively quickly.

3.4. Understanding the North Pacific Cooling: Oceanic and Atmospheric Feedbacks

The strong cooling of the North Pacific in response to the addition of black carbon naturally leads to questions about the mechanisms involved in such a counterintuitive response to a warming aerosol. We compare the atmosphere-only and coupled surface heat balances in the last two columns of Table 1. While the incoming shortwave radiation to the North Pacific Ocean declines by 5.7 W m $^{-2}$, this decline is more than balanced by a decrease in the net longwave, sensible, and evaporative cooling of the ocean, which result in a net heating of the ocean of 8.7 W m $^{-2}$. This means reduction in ocean heat transport corresponding to a drop of about 3 W m^{-2} is necessary to maintain the cooling. In the absence of such a decrease in heat supply the net heat flux into the ocean would damp out the temperature anomaly within a year.

As shown in Figure 2, a net inflow of water to the North Pacific occurs at middle depths and is redistributed into a surface return flow (shown by the counterclockwise circulation in Figure 2a and the southward near-surface flow in Figure 2b) and a deep return flow (shown by the clockwise circulation in Figure 2a and the southward flow below 400 m on both the western and eastern boundaries). Both loops involve southward flows that are cooler than the northward inflow in the eastern Pacific. Time series of the deeper branch of this loop (the North Pacific overturning circulation at 45°N, Figure 8c) shows that this circulation is initially stronger but then declines by 0.6 Sv. However, as is clear from Figure 2, overturning in depth space is a somewhat flawed metric for heat transport as warm water enters the subpolar North Pacific on the east, while cold water exits on the west.

The green line in Figure 8c shows the change in the influx of water warmer than 6°C. The time series of warm water inflow has a much better relationship with the surface temperatures and low clouds (correlation of 0.67 and −0.59, respectively) than does the overturning (correlation of 0.35 and −0.11 respectively). Examination of net water fluxes shows that the inflow of water warmer than 6°C drops from 5.3 to 4.4 Sv, a total of

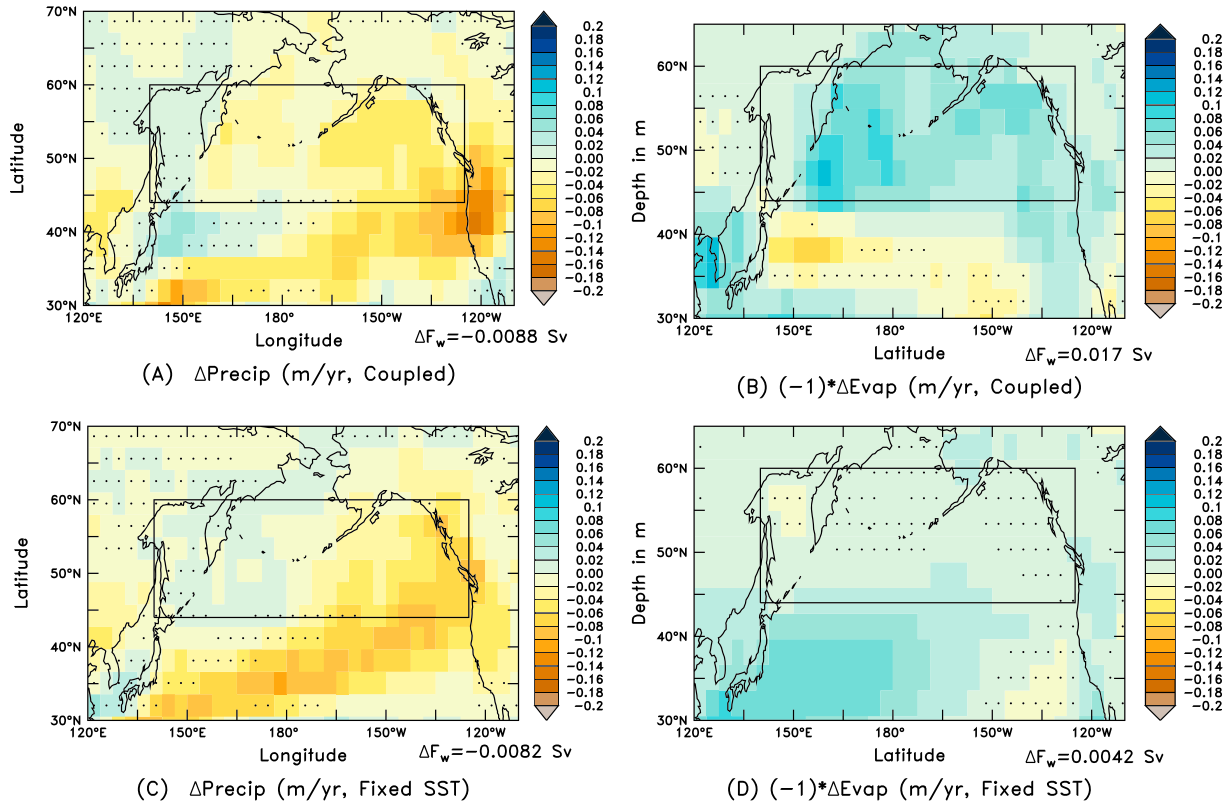

Figure 10. Changes in the freshwater fluxes due to step change in black carbon. Numbers to lower right show net change in water flux to ocean within the box in the figure (corresponding to the North Pacific region). Dots denote points where local changes are not significant at the 95% confidence level (though when averaged regionally results are significant). (a) Precipitation, coupled simulations. (b) (−1)× Evaporation, coupled simulations. (c) Precipitation, fixed SST simulations. (d) (−1)× Evaporation, fixed SST simulations.

about 17%. The outflow of water colder than 6°C drops by about 0.1 Sv in the top 100 m, and 0.8 Sv below this, so that it is the decline in the formation of intermediate water that is most important. This slowdown in both the upper and lower loops produces a decrease in the advective heat transport across 44°N that corresponds to a net cooling of 3.4 W m $^{-2}$, somewhat larger than the 3 W m^{-2} we need to balance the changes in surface fluxes. However, an increase in the diffusive heat transport (resulting from the larger gradient in temperature between the subpolar and subtropical gyres) results in an additional flux of 0.4 W m^{-2}, allowing us to close our heat budgets.

A rough comparison between the change in ocean heat transport and the fixed SST change in shortwave cooling suggests that these factors are roughly equally responsible for the 0.52 K cooling of the North Pacific. This can be shown more quantitatively by looking more carefully at the net heat balance. Assuming that the changes in all fluxes are proportional to the change in temperature, we can break the heat balance down into a component associated with the shortwave response to fixed SST F_{SW}^{fixed}, and components of shortwave and ocean heat transport that linearly increase with SST so that

$$F_{SW}^{fixed} + \lambda_{SW} \times \Delta T + \lambda_{OHT} \times \Delta T + \lambda_{nonsolar} \times \Delta T = 0 \quad (2)$$

where the coefficients $\lambda_{SW,OHT,nonsolar}$ refer to the change in the net shortwave, ocean heat transport, and sum of sensible, latent, and net longwave fluxes resulting from a 1 K change in SST. Given a cooling $\Delta T = -0.52$ K, the additional -2.7 W m^{-2} associated with coupling gives us $\lambda_{SW} = -5.3$ W m^{-2} K^{-1}. Similarly, $\lambda_{OHT} = -5.8$ Wm^{-2}K^{-1}, and $\lambda_{nonsolar}$=16.8 W m^{-2} K^{-1}. Both λ_{SW} and $\lambda_{nonsolar}$ are similar to the values found in the Southern Ocean by Seviour et al. (2017) in a different experiment with the same coupled model. In the absence of a change in ocean heat transport such as might be found in a slab model (i.e., if $\lambda_{OHT} = 0$), the expected change in temperature would then be $F_{SW}^{fixed}/(\lambda_{SW} + \lambda_{nonsolar})$, which is −0.26 K.

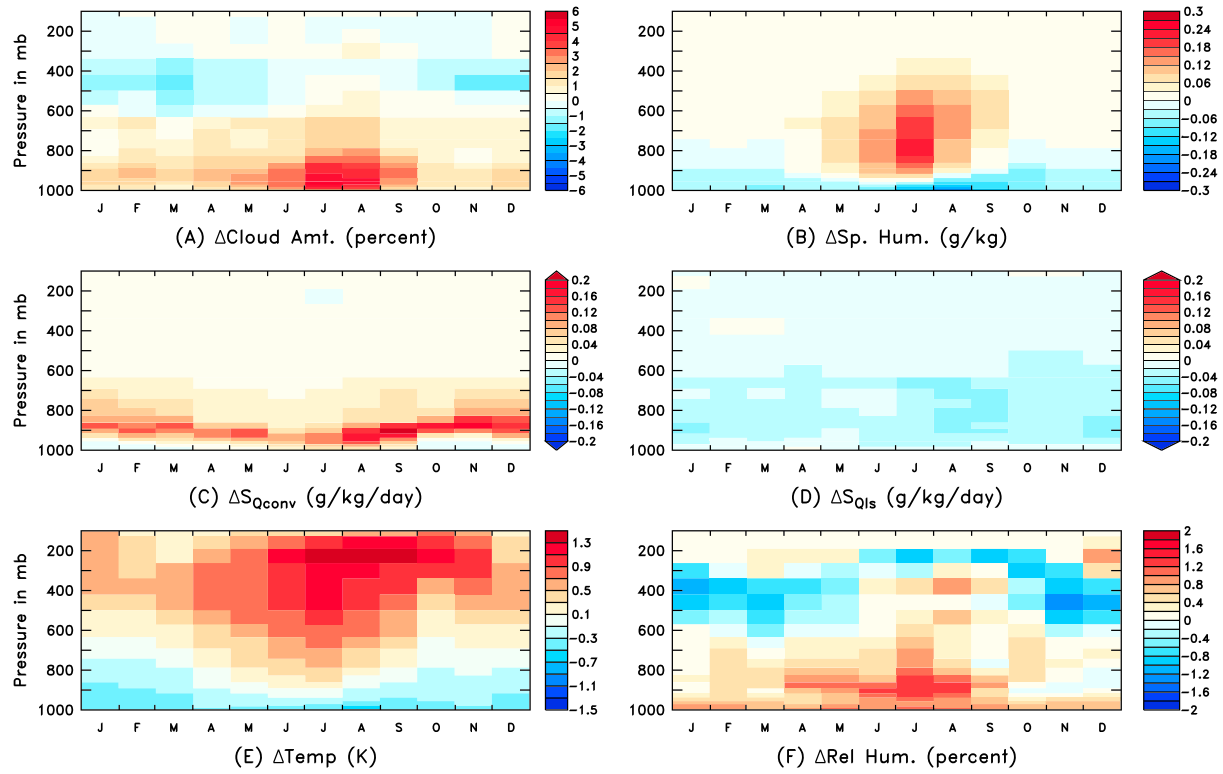

Figure 11. Annual cycle of changes over the subpolar North Pacific box (150°E–125°W, 44–60°N) in coupled simulation. (a) Heating rate due to cumulus convection in K/d. (b) Heating rate due to stratiform convection in K/d. (c) Total cloud amount in percent. (d) Specific humidity in g/kg. (e) Temperature in K. (f) Relative humidity in percent.

We now turn to the question of what causes the change in overturning. One might expect that the near-surface atmospheric cooling seen in Figure 3c would lead to an increase in density and thus an increase rather than a decrease in overturning. Indeed, this seems to occur during the first few decades of the perturbation run. However, on longer time scales the sea surface salinity (Figure 9a) drops along the edges of the subpolar gyre. When a zonal average is taken, the resulting contrast between the surface and intermediate depths increases by 25% from 0.31 to 0.40 practical salinity unit. This in turn increases the density stratification making it harder to form intermediate water and slowing the overturning.

It is interesting to compare these changes to those found in the 2013 World Ocean Atlas between decades centered around 2000 and 1970 (Figures 9c and 9d), recognizing that the observed patterns of change will reflect greenhouse gas forcing, sulfate aerosol forcing, and natural variability as well as change in black carbon aerosols. The observed change in sea surface salinity (Figure 9c) shows a similar pattern of freshening along the southern edge of the subpolar gyre and salinification in the Bering Sea but rather different patterns in the subtropical gyre and in coastal regions. Similarly, the observations show a somewhat smaller freshening of the southern subpolar gyre in the observations relative to the coupled model, with a penetration of a saltier signal from the north. Given the lack of comparability between the observations and the models, one should not be too surprised to find differences, but it is instructive that the salinity changes associated with changing black carbon in the model are often larger than the historical changes—implying that black carbon could play a role in determining the modern salinity structure.

The net change in the inflow of relatively salty warm waters and outflow of fresher cold waters noted above would be expected to change the salinity gradient by 17%. Changes in flow thus greatly magnify the relatively small increase (5%) in surface freshwater flux from 0.125 to 0.131 Sv over the North Pacific from 44 to 60°N. The precipitation (Figure 10a) actually decreases over this region by 0.0088 Sv, so that the key driver of the change in freshwater flux is a drop of the evaporation by 0.017 Sv (Figure 10b). The change in precipitation in the coupled simulations is very similar to that found in the fixed SST simulations (Figure 10c) but the change in evaporation, while of the same sign, is much larger. Indeed, in the fixed SST simulations, the prediction

is that the ocean would become saltier rather than fresher. It is only when cooling SSTs reduce the saturation vapor pressures at the ocean surface that the evaporative flux drops, by an average of about 3 cm yr^{-1} over the box shown in Figure 10.

We would not expect that a reduction in evaporation would be associated with an increase in cloudiness. Examining the seasonal cycle of heating from cumulus and stratiform convection over the North Pacific (Figures 11a and 11b), we see a general decrease in cumulus cloud heating throughout the year and an increase in stratiform cloud heating. The pattern of change in cloud amount (Figure 11c) shows a general increase in the region where stratiform cloud heating is increasing, although the seasonal cycle of change is much more pronounced. The specific humidity (Figure 11c) shows a decline near the surface, as would be expected from previous results, but a marked increase aloft during the summer months. Temperature (Figure 11c) shows a similar pattern in the lower troposphere. Because the near-surface temperature reduces the saturation-specific humidity more than the specific humidity, the relative humidity (Figure 11c) increases below 800 mbar, matching the change in clouds much better than any of the other fields. The fixed SST model (Figure S2) shows very similar patterns for temperature and specific humidity in the upper atmosphere, but by definition cannot capture the near-surface cooling. As a result the changes in relative humidity and clouds are much attenuated.

4. Conclusion and Discussion

As suggested by previous work, our results show that adding a realistic distribution of black carbon to the atmosphere warms the planet as a whole. However, the pattern of surface air temperature changes is not proportional to the local black carbon aerosol concentration with the largest surface air temperature changes seen away from the regions with the largest aerosol burden. In one such region (the subpolar North Pacific), adding black carbon actually produces a net cooling. This is despite the fact that increased black carbon always results in an increase in shortwave heating of the atmosphere that is highly correlated with the column burden. Four key processes appear to play a role in explaining this lack of relationship between anomalous atmospheric heating and surface temperature change. The first is that some of the heat absorbed by the aerosols would otherwise have been absorbed by the ground and diffused upward. Changing the pathway by which heat reaches the lower atmosphere has little impact on the temperature. Second, as noted by previous investigators (Allen & Sherwood, 2010; Persad et al., 2011; Randles et al., 2013) changes in aerosol heating produce changes in atmospheric stability, which can have different impacts on the radiative balance depending on the region. Third, a general moistening of the boundary in the presence of black carbon reduces evaporative cooling of the surface. Finally, changes in the oceanic transport of heat, particularly within the subpolar North Pacific, can significantly magnify the impact of cloud feedbacks.

Although black carbon-induced warming aloft increases stability over the surface and reduces deep convection nearly everywhere, the temperature response differs depending on the presence of an ocean and the use of a fully coupled atmosphere-ocean model. Over the ocean, the increase in relative humidity produced by the decline in surface air temperature in the presence of a moisture source means that more stratiform clouds form — reinforcing the surface cooling. In the North Pacific the resulting decrease in evaporation also causes a decrease in surface salinity, increasing density stratification and slowing the overturning that supplies warm water to subpolar latitudes. This effect is similar in magnitude to the uncoupled change in downwelling shortwave radiation. The behavior over the ocean is in contrast to land regimes, where the suppression of deep convection and warming of the surface do not result in more clouds.

The proposed oceanic response is a positive feedback mechanism: as the surface cools, relative humidity and cloudiness increase, further reducing shortwave heating and the decrease in salinity produces a weaker oceanic heat supply. Whether this mechanism is in fact found in the real world will depend on the accuracy of models in simulating overturning in this region. It is possible that our model, with relatively weak initial stratification, has too strong an initial overturning circulation and thus too strong a sensitivity to ocean circulation. On the other hand, the transformation rates of water masses that we find are actually smaller than those estimated by Talley (1999). Moreover, as noted in Gnanadesikan et al. (2013), many Earth System models are unable to simulate observations of poorly oxygenated waters at relatively shallow depths in the subpolar North Pacific, most likely because they also predict overly strong ventilation of the intermediate waters. This means that if our model is too sensitive, a similar bias may be found in others.

The possibility for black carbon to have significant climate effects far from a source region is not novel; for example, Ramanathan and Carmichael (2008) have emphasized the importance of aerosol transport. However, the location and strength of our signal appears to be new and differs from transient simulations such as those reported in Ocko et al. (2012, 2014). The large interdecadal variability we see in our simulations illustrates the challenges for such short, transient simulations in distinguishing response to decadal changes in black carbon from natural variability and suggests that ensembles of transient simulations may be necessary to extract the true impact of black carbon.

Caution must be exercised when extrapolating from these results to the real world as they could depend on cloud parameterization. Indeed, recent work has linked black carbon aerosols with increases in deep convective clouds rather than stratiform decks, though many studies that do so are either regional studies that neglect the impact of climate feedbacks (e.g., Zhang et al., 2007) or are run as fixed SST experiments that ignore the role of oceanic processes (e.g., Wang et al., 2014), making direct comparisons to our results difficult. Similar experiments in other fully coupled models including aerosol-cloud interactions would help to clarify this issue.

A particular aspect of cloud parameterization that plays an important role in our results is the positive relationship between stability and low clouds (Klein & Hartmann, 1993; Norris et al., 1998), which is not shared by all climate models. Recent results (Clement et al., 2009; Ferreira et al., 2015; Grise & Polvani, 2014; Seviour et al., 2017; Zhu et al., 2007) suggest that Community Earth System Model family reacts to increased atmospheric stability by decreasing cloudiness, while the Geophysical Fluid Dynamics Laboratory (GFDL) model family reacts by increasing cloudiness. This is likely because of details in how the boundary layer, deep convection, and large-scale cloud scheme interact. Increasing deep convection produces both downwelling (which stabilizes the boundary layer) and turbulence (which destabilizes the boundary layer)—these processes likely have different magnitudes in different schemes. Clement et al. (2009) indicate that the net positive feedback is more consistent with observations for stratocumulus clouds over the northeast Pacific, and Grise and Polvani (2014) suggest that it is more consistent with observations over the Southern Ocean. Our results should motivate a careful observational exploration of stratus cloud-SST linkages over the subpolar North Pacific.

Despite the potential sensitivities of our results to model details, this work does point to the importance of evaluating aerosol feedbacks in a fully coupled framework. Allowing the sea surface temperatures and ocean heat transport to change can alter temperature responses from cooling to warming (as over north central Asia) or greatly magnify the impacts of radiative forcing (as over the North Pacific). Isolating such impacts, however, will require relatively long "Green's function" runs such as those done here in which a step function change is integrated for a long time, or an ensemble of historical simulations. In single, relatively short historical simulations the signal of interannual variability may otherwise overwhelm regional responses.

Acknowledgments
This work was funded in part by NSF IGERT grants DGE-1069213, EAR-1135382 and FESD-1338814. Special thanks to Cynthia Randles, Marcus Sarofim, Valentina Aquila, and two anonymous reviewers for helpful suggestions. The data from this experiment are available in netCDF format at https://jh.app.box.com/s/s9lfnh19ouijkjddedy3.

References

Allen, R. J., & Sherwood, S. C. (2010). Aerosol-cloud semi-direct effect and land-sea temperature contrast in a GCM. *Geophysical Research Letters*, *37*, L07702. https://doi.org/10.1029/2010GL042759

Anderson, J. L., Balaji, V., Broccoli, A. J., Cooke, W. F., Delworth, T. L., Dixon, K. W., … Wyman, L. (2004). The new GFDL global atmosphere and land model AM2-LM2: Evaluation with prescribed SST simulations. *Journal of Climate*, *17*(24), 4641–4673.

Bond, T. C., Doherty, S. J., Fahey, D. W., Forster, P. M., Berntsen, T., DeAngelo, B. J., … Zender, C. S. (2013). Bounding the role of black carbon in the climate system: A scientific assessment. *Journal of Geophysical Research: Atmospheres*, *118*, 5380–5552. https://doi.org/10.1002/jgrd.50171

Brioude, J., Cooper, O. R., Feingold, G., Trainer, M., Freitas, S. R., Kowal, D., … Hsie, E.-Y. (2009). Effect of biomass burning on marine stratocumulus clouds off the California coast. *Atmospheric Chemistry and Physics*, *9*, 8841–8856. https://doi.org/10.5194/acp-9-8841-2009

Clement, A. C., Burgman R., & Norris, J. (2009). Observational and model evidence for positive low-level cloud feedback. *Science*, *325*, 460–446. https://doi.org/10.1126/science.1171255

Cooke, W. F., Liousse, C., Cachier, H., & Feichter, J. (1999). Construction of a 1°×1° fossil fuel emission data set for carbonaceous aerosol and implementation and radiative impact in the ECHAM4 model. *Journal of Geophysical Research: Atmospheres*, *104*(D18), 22,137–22,162. https://doi.org/10.1029/1999JD900187

Dunne, J. P., John, J. G., Adcroft, A. J., Griffies, S. M., Hallberg, R. W., Shevliakova, E., … Zadeh, N. (2012). GFDL's ESM2 global coupled climate–carbon Earth System Models. Part I: Physical formulation and baseline simulation characteristics. *Journal of Climate*, *25*(19), 6646–6665. https://doi.org/10.1175/JCLI-D-11-00560.1

Ferreira, D., Marshall, J., Bitz, C. M., Solomon, S., & Plumb, A. (2015). Antarctic ocean and sea ice response to ozone depletion: A two-time-scale problem. *Journal of Climate*, *28*, 1206–1226. https://doi.org/10.1175/JCLI-D-14-00313.1

Galbraith, E. D., Kwon, E. Y., Gnanadesikan, A., Rodgers, K. B., Griffies, S. M., Bianchi, D., … Isaac, M. (2011). Climate variability and radiocarbon in the CM2Mc Earth system model. *Journal of Climate*, *24*(16), 4230–4254.

Ginoux, P., Horowitz, L. W., Ramaswamy, V., Geogdzhayev, I. V., Holben, B. N., Stenchikov, G., & Tie, X. (2006). Evaluation of aerosol distribution and optical depth in the geophysical fluid dynamics laboratory coupled model CM2.1 for present climate. *Journal of Geophysical Research*, *111*, D22210. https://doi.org/10.1029/2005JD006707

Gnanadesikan, A., Bianchi, D., & Pradal, M.-A. (2013). Critical role for mesoscale eddy diffusion in supplying oxygen to hypoxic ocean waters. *Geophysical Research Letters*, *40*, 5194–5198. https://doi.org/10.1002/grl.50998

Gnanadesikan, A., Dixon, K. W., Griffies, S. M., Balaji, V., Barreiro, M., Beesley, J. A., … John, P. (2006). GFDL's CM2 global coupled climate models. Part II: The baseline ocean simulation. *Journal of Climate*, *19*(5), 675–697.

Griffies, S., Gnanadesikan, A., Dixon, K. W., Dunne, J., Gerdes, R., Harrison, M. J., … Zhang, R. (2005). Formulation of an ocean model for global climate simulations. *Ocean Science*, *1*(1), 45–79.

Grise, K. M., & Polvani, L. M. (2014). Southern Hemisphere cloud dynamics biases in CMIP5 models and their implications for climate projections. *Journal of Climate*, *27*, 6074–6092. https://doi.org/10.1175/JCLI-D-14-00113.1

Horowitz, L. W., Walters, S., Mauzerall, D. L., Emmons, L. K., Rasch, P. J., Granier, C., … Brasseur, G. P. (2003). A global simulation of tropospheric ozone and related tracers: Description and evaluation of MOZART, version 2. *Journal of Geophysical Research*, *108*(D24), 4784. https://doi.org/10.1029/2002JD002853

Jakob, C., & Klein, S. A. (2000). A parametrization of the effects of cloud and precipitation overlap for use in general-circulation models. *Quarterly Journal of the Royal Meteorological Society*, *126*(568), 2525–2544.

Keil, A., & Haywood, J. M. (2003). Solar radiative forcing by biomass burning aerosol particles during SAFARI 2000: A case study based on measured aerosol and cloud properties. *Journal of Geophysical Research*, *108*(D13), 8467. https://doi.org/doi:10.1029/2002JD002315

Klein, S. A., & Hartmann, D. L. (1993). The seasonal cycle of low stratiform clouds. *Journal of Climate*, *6*(8), 1587–1606. https://doi.org/10.1175/1520-0442(1993)006<1587:TSCOLS>2.0.CO;2

Koch, D., Bauer, S. E., Del Genio, A., Faluvegi, G., McConnell, J. R., Menon, S., … Shindell, D. (2011). Coupled aerosol-chemistry-climate twentieth-century transient model investigation: Trends in short-lived species and climate responses. *Journal of Climate*, *24*(11), 2693–2714. https://doi.org/10.1175/2011JCLI3582.1

Locarnini, R. A., Mishonov, A. V., Antonov, J. I., Boyer, T. P., Garcia, H. E., Baranova, O. K., … Seidov, D. (2013). *World ocean atlas 2013*. In S. Levitus, A. Mishonov, & Technical: NOAA Atlas NESDIS 73 (Eds.), *Volume 1: Temperature* (40 pp.). Silver Spring, MD.

Meehl, G. A., Arblaster, J. M., & Collins, W. D. (2008). Effects of black carbon aerosols on the Indian monsoon. *Journal of Climate*, *21*(12), 2869–2882.

Moorthi, S., & Suarez, M. J. (1992). Relaxed Arakawa-Schubert. A parameterization of moist convection for general circulation models. *Monthly Weather Review*, *120*(6), 978–1002.

Norris, J. R., Zhang, Y., & Wallace, J. M. (1998). Role of low clouds in summertime atmosphere–ocean interactions over the North Pacific. *Journal of Climate*, *11*(10), 2482–2490. https://doi.org/10.1175/1520-0442(1998)011<2482:ROLCIS>2.0.CO;2

Ocko, I. B., Ramaswamy, V., Ginoux, P., Ming, Y., & Horowitz, L. W. (2012). Sensitivity of scattering and absorbing aerosol direct radiative forcing to physical climate factors. *Journal of Geophysical Research*, *117*, D20203. https://doi.org/10.1029/2012JD018019

Ocko, I. B., Ramaswamy, V., & Ming, Y. (2014). Contrasting climate responses to the scattering and absorbing features of anthropogenic aerosol forcings. *Journal of Climate*, *27*, 5329–5345. https://doi.org/10.1175/JCLI-D-13-00401.1

Persad, G. G., Ming, Y., & Ramaswamy, V. (2011). Tropical tropospheric-only responses to absorbing aerosols. *Journal of Climate*, *25*(7), 2471–2480. https://doi.org/10.1175/JCLI-D-11-00122.1

Seager, R., Kushnir, Y., Herweijer, C., Naik, N., & Velez, J. (2005). Modeling of tropical forcing of persistent droughts and Pluvials over western north America: 1856–2000. *Journal of Climate*, *18*, 4065–4088. https://doi.org/10.1175/JCLI3522.1

Ramanathan, V., & Carmichael, G. (2008). Global and regional climate changes due to black carbon. *Nature Geoscience*, *1*(4), 221–227.

Ramanathan, V., Chung, C., Kim, D., Bettge, T., Buja, L., Kiehl, J. T., … Wild, M. (2005). Atmospheric brown clouds: Impacts on South Asian climate and hydrological cycle. *Proceedings of the National Academy of Sciences of the United States of America*, *102*(15), 5326–5333. https://doi.org/10.1073/pnas.0500656102

Randles, C. A., Colarco, P. R., & da Silva, A. (2013). Direct and semi-direct aerosol effects in the NASA GEOS-5 AGCM: Aerosol-climate interactions due to prognostic versus prescribed aerosols. *Journal of Geophysical Research: Atmospheres*, *118*, 149–169. https://doi.org/10.1029/2012JD018388

Roeckner, E., Stier, P., Feichter, J., Kloster, S., Esch, M., & Fischer-Bruns, I. (2006). Impact of carbonaceous aerosol emissions on regional climate change. *Climate Dynamics*, *27*(6), 553–571.

Rotstayn, L. D. (1997). A physically based scheme for the treatment of stratiform clouds and precipitation in large-scale models. I: Description and evaluation of the microphysical processes. *Quarterly Journal of the Royal Meteorological Society*, *123*(541), 1227–1282.

Rotstayn, L. D., Ryan, B. F., & Katzfey, J. J. (2000). A scheme for calculation of the liquid fraction in mixed-phase stratiform clouds in large-scale models. *Monthly Weather Review*, *128*(4), 1070–1088.

Samset, M. G., Samset, B. H., Myhre, G., Herber, A., Kondo, Y., & Li, S.-M. (2014). Modeled black carbon radiative forcing and atmospheric lifetime in Aerocom phase II constrained by aircraft observations. *Atmospheric Chemistry and Physics Discussions*, *14*, 20,083–20,115.

Seviour, W. J. M., Gnanadesikan, A., Waugh, D., & Pradal, M. A. (2017). Transient response of the Southern Ocean to changing ozone: Regional responses and physical mechanisms. *Journal of Climate*, *30*, 2463–2480.

Shindell, D., Schulz, M., Ming, Y., Takemura, T., Faluvegi, G., & Ramaswamy, V. (2010). Spatial scales of climate response to inhomogeneous radiative forcing. *Journal of Geophysical Research*, *115*, D19110. https://doi.org/10.1029/2010JD014108

Talley, L. D. (1999). Some aspects of ocean heat transport by the shallow, intermediate and deep overturning circulations. In P. U. Clark, R. S. Webb, & L. D. Keigwin (Eds.), *Mechanisms of Global Climate Change at Millennial Time Scales*. Washington, DC: American Geophysical Union. https://doi.org/10.1029/GM112p0001

Trossman, D. S., Palter, J. B., Merlis, T. M., Huang, Y., & Xia, Y. (2016). Large-scale ocean circulation-cloud interactions reduce the pace of transient climate change. *Geophysical Research Letters*, *43*, 3935–3943. https://doi.org/10.1002/2016GL067931

Wang, C., Kim, D., Ekman, A. M., Barth, M. C., & Rasch, P. J. (2009). Impact of anthropogenic aerosols on Indian summer monsoon. *Geophysical Research Letters*, *36*, L21704. https://doi.org/10.1029/2009GL040114

Wang, Y., Wang, M., Zhang, R., Ghan, S. J., Lin, Y., Hu, J., … Molina, M. J. (2014). Assessing the effects of anthropogenic aerosols on Pacific storm track using a multiscale global climate model. *Proceedings of the National Academy of Sciences*, *111*(19), 6894–6899. https://doi.org/10.1073/pnas.1403364111

Winton, M. (2003). On the climatic impact of ocean circulation. *Journal of Climate*, *16*(17), 2875–2889. https://doi.org/10.1175/1520-0442(2003)016<2875:OTCIOO>2.0.CO;2

Zhang, R., Li, G., Fan, J., Wu, D. L., & Molina, M. J. (2007). Intensification of Pacific storm track linked to Asian pollution. *Proceedings of the National Academy of Sciences*, *104*(13), 5295–5299. https://doi.org/10.1073/pnas.0700618104

Zhu, P., Hack, J. J., & Kiehl, J. T. (2007). Diagnosing cloud feedbacks in general circulation models. *Journal of Climate*, *20*, 2602–2622. https://doi.org/10.1175/JCLI4140.1

Zweng, M. M., Reagan, J. J. R., Antonov, I., Locarnini, R. A., Mishonov, A. V., Boyer, T. P., … Biddle, M. M. (2013). *World ocean atlas 2013*. In S. Levitus, A. Mishonov, & Technical: NOAA Atlas NESDIS 74 (Eds.), *Volume 2: Salinity* (39 pp.). Silver Spring, MD.